# Peculiar half-metallic state in zigzag nanoribbons of $MoS_2$: Spin filtering

F. Khoeini,[1] Kh. Shakouri,[2,3,*] and F. M. Peeters[2]
[1]*Department of Physics, University of Zanjan, P.O. Box 45195-313, Zanjan, Iran*
[2]*Departement Fysica, Universiteit Antwerpen, Groenenborgerlaan 171, B-2020 Antwerpen, Belgium*
[3]*Gorlaeus Laboratories, Leiden Institute of Chemistry, Leiden University, P.O. Box 9502, 2300 RA Leiden, The Netherlands*
(Received 6 July 2016; revised manuscript received 12 August 2016; published 9 September 2016)

Layered structures of molybdenum disulfide ($MoS_2$) belong to a new class of two-dimensional (2D) semiconductor materials in which monolayers exhibit a direct band gap in their electronic spectrum. This band gap has recently been shown to vanish due to the presence of metallic edge modes when $MoS_2$ monolayers are terminated by zigzag edges on both sides. Here, we demonstrate that a zigzag nanoribbon of $MoS_2$, when exposed to an external exchange field in combination with a transverse electric field, has the potential to exhibit a peculiar half-metallic nature and thereby allows electrons of only one spin direction to move. The peculiarity of such spin-selective conductors originates from a spin switch near the gap-closing region, so the allowed spin orientation can be controlled by means of an external gate voltage. It is shown that the induced half-metallic phase is resistant to random fluctuations of the exchange field as well as the presence of edge vacancies.

DOI: 10.1103/PhysRevB.94.125412

## I. INTRODUCTION

Since the synthesis of graphene [1,2], substantial efforts have been made to integrate novel physical properties of two-dimensional (2D) materials in order to pave the way for an adaptable, ultrafast, low-power spintronics. While group-IV allotropes, in particular those made out of carbon atoms, are still the most widely studied structures to date, chemically stable monolayers of transition-metal dichalcogenides (TMDCs) have received increasing attention recently. The reason stems from their inherent direct band gap [3–5] and large spin-orbit interaction [6], which render them potential candidates for optospintronics and transistor applications. By taking advantage of the optical band gap of monolayer TMDCs, 2D nanoelectronic devices such as ultrasensitive photodetectors [7] and field-effect transistors [8] have already been realized experimentally for $MoS_2$ monolayers.

The ability to achieve a high-mobility TMDC for use in 2D transistors is of fundamental and technological importance. The encapsulation of $MoS_2$ by a strong dielectric material has been shown to increase substantially its carrier mobility [9]. Furthermore, most features observed in $MoS_2$-based devices [8,10,11] are complementary to former transistors, differentiating it from other TMDCs. The transmission of charge carriers in $MoS_2$ monolayers is performed via Mo atoms, which are heavier than carbon atoms. The combination of this property of Mo with the fact that $MoS_2$ lacks inversion symmetry results in a strong spin-orbit coupling of about 0.15 eV in the valence band [6,12]. As a consequence of the coexistence of spin-orbit interaction and inversion symmetry breaking, an interesting spin-valley coupling can be observed in $MoS_2$ monolayers, resulting in novel physics [13].

Edge-structure engineering of 2D crystalline materials is often a key strategy to control their electronic and transport properties. Likewise, the electrical properties of $MoS_2$ are strongly edge dependent, ranging from insulating to metallic for armchair- and zigzag-terminated edges, respectively [14]. The existence of metallic edge states in monolayers of $MoS_2$ has recently been confirmed experimentally [15], which is consistent with earlier theoretical predictions [12,16,17]. Interestingly, the conductive edge modes of zigzag $MoS_2$ nanoribbons (ZMDSNs) are shown to mimic the physics of massless Dirac fermions near the gap-closing point [18,19]. It was predicted that a strongly gated ZMDSN is forced topologically into a nontrivial superconducting regime [20]. In addition, it was predicted that a ZMDSN, as well as other zigzag monolayers of TMDCs, can exhibit zero-energy modes when in proximity to an *s*-wave superconductor and an in-plane magnetic field [21], revealing their potential for hosting Majorana bound states. Another notable feature of ZMDSNs, which is addressed in this paper, is that they can act as a spin-selective conductor. Consequently, the $MoS_2$ nanoribbon allows just electrons of one spin direction to propagate, while for the remainder it behaves like an insulator. To this end, we consider the influence of a transverse electric field together with a nonlocal exchange field. In response to a transverse electric field the behavior of ZMDSNs is twofold and can offer either semiconducting or metallic properties. Nevertheless, the edge states in either case possess a right-handed helicity, and hence the spin of each particle is in the same direction as its momentum. By adding an exchange field in combination with a transverse electric field we show that ZMDSNs can be converted to a peculiar half-metal system. The main property of such half-metal systems is that the allowed spin orientation can be controlled near the gap-closing region. It will also be demonstrated that the induced half-metallicity is resistant to small fluctuations of the exchange field or the existence of edge vacancies.

This paper is organized as follows. In Sec. II, we present our model, which is used to calculate the electronic structure as well as the quantum transport properties. In Sec. III, we focus on possible mechanisms that allow us to induce a perfect spin gap in the band structure of ZMDSNs. Different physical aspects of the present work are elaborated in this section. We conclude with a summary in Sec. IV.

*k.shakouri@lic.leidenuniv.nl

 

## II. THEORETICAL MODEL

### A. Multiband tight-binding Hamiltonian

The electronic structure of a monolayer $MoS_2$ in the entire Brillouin zone can be described by a multiband tight-binding formalism derived from first-principles calculations. The most comprehensive model introduced heretofore accounts for 11 bands, including $d$ and $p$ orbitals of Mo and S atoms, respectively [22]. By performing an appropriate unitary transformation based on parity considerations with respect to the out-of-plane ($z$) axis [23,24], the contribution of $p$ orbitals of nonplanar S layers can be cast into symmetric and antisymmetric combinations. This allows us to describe the Hamiltonian in a reduced atomic orbital basis as ($d_{z^2}$, $d_{x^2-y^2}$, $d_{xy}$) for Mo and [$\frac{1}{\sqrt{2}}(p_x^t + p_x^b)$, $\frac{1}{\sqrt{2}}(p_y^t + p_y^b)$, $\frac{1}{\sqrt{2}}(p_z^t - p_z^b)$] for S atoms, where $t$ and $b$ refer to the top and bottom S layers, respectively. Considering the effect of local spin-orbit couplings, the Hamiltonian can be written in real space as [24]

$$\begin{aligned} H = & \sum_{i,\mu} \varepsilon_{i,\mu}^{M} c_{i,\mu}^{\dagger} c_{i,\mu} + \varepsilon_{i,\mu}^{S} b_{i,\mu}^{\dagger} b_{i,\mu} \\ & + \sum_{\langle\langle ij\rangle\rangle,\mu\nu} \left( t_{ij,\mu\nu}^{MM} c_{i,\mu}^{\dagger} c_{j,\nu} + t_{ij,\mu\nu}^{SS} b_{i,\mu}^{\dagger} b_{j,\nu} \right) \\ & + \sum_{\langle ij\rangle,\mu\nu} t_{ij,\mu\nu}^{MS} c_{i,\mu}^{\dagger} b_{j,\nu} + \text{H.c.}, \end{aligned} \tag{1}$$

where $i, j$ and $\mu, \nu$ run over the lattice sites and atomic orbital bases, respectively, $c_{i,\mu}$ ($b_{i,\nu}$) is the annihilation operator for Mo (S), and, correspondingly, $c_{i,\mu}^{\dagger}$ ($b_{i,\nu}^{\dagger}$) is the creation operator. The hopping coefficients $t_{ij,\mu\nu}^{MM}$, $t_{ij,\mu\nu}^{MS}$, and $t_{ij,\mu\nu}^{SS}$ are determined based on the hopping directions shown in Fig. 1(a), as detailed in Table I. Meanwhile, in the presence of a uniform exchange term $h$, the on-site Hamiltonians of Mo and S atoms are given by

$$\varepsilon_i^M = \begin{bmatrix} \Delta_0 & 0 & 0 \\ 0 & \Delta_2 & -is\lambda_M \\ 0 & is\lambda_M & \Delta_2 \end{bmatrix} - hs\mathbf{I} \tag{2}$$

and

$$\varepsilon_i^S = \begin{bmatrix} \Delta_p + t_{xx}^{\perp} & -\frac{1}{2}is\lambda_S & 0 \\ \frac{1}{2}is\lambda_S & \Delta_p + t_{yy}^{\perp} & 0 \\ 0 & 0 & \Delta_z - t_{zz}^{\perp} \end{bmatrix} - hs\mathbf{I}, \tag{3}$$

respectively. In Eqs. (2) and (3), $\lambda_M = 0.075$ eV and $\lambda_S = 0.052$ eV represent the strengths of spin-orbit interactions for Mo and S [26], respectively, $\mathbf{I}$ is the identity matrix, and $s$ is the spin angular momentum along the $z$ axis. Furthermore, the vertical hopping between the top and bottom sulfur sheets is denoted by $t_{vv}^{\perp}$ ($v = x, y, z$). Other tight-binding parameters such as $\Delta_0$ are given in Table II. Note that the exchange field in 2D materials can be induced by proximity to a ferromagnetic insulator substrate (for instance, see Refs. [27–31] and references therein).

For the case of an endless ZMDSN, the periodicity of the honeycomb structure is maintained along its extension direction. Strictly speaking, such perfect systems can be viewed as a linear chain of periodically repeated primitive cells, each of which consists of a small armchair array of Mo-S bonds [see the unit cell specified in Fig. 1(a)]. Therefore, the crystal momentum associated with the longitudinal direction $\hat{x}$ is a good quantum number, i.e., $[H, p_x] = 0$, which allows us to use Bloch's theorem. Considering the interaction of each primitive cell with the next or previous one, which we denote here as $H_{l,l+1}$ and $H_{l,l-1} = H_{l,l+1}^{\dagger}$, respectively, the $k_x$-dependent Hamiltonian can be expressed as

$$H(k_x) = H_{l,l+1} e^{ik_x a} + H_{l,l} + H_{l,l+1}^{\dagger} e^{-ik_x a}, \tag{4}$$

where $H_{l,l}$ comprises only interior interactions of the $l$th unit cell and $a = 0.316$ nm is the lattice constant.

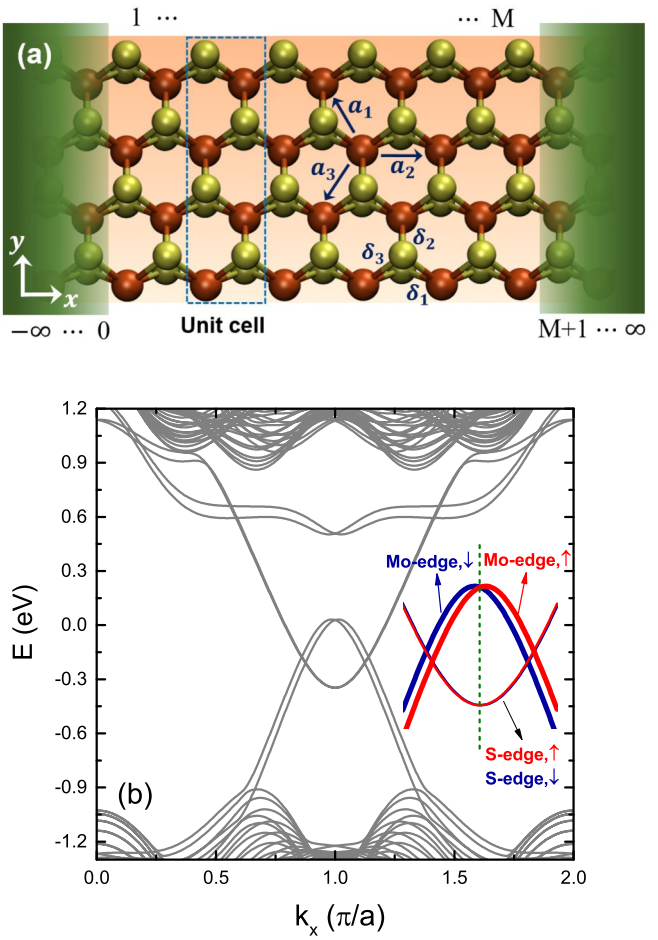


FIG. 1. (a) Schematic illustration of the structure of a ZMDSN as the central channel of a spintronic nanodevice. $a_i$ and $\delta_i$ indicate the direction of nearest hoppings between homogeneous (Mo-Mo or S-S) and inhomogeneous (Mo-S) atoms, respectively. The channel region consists of $M$ unit cells extended along the longitudinal direction. Each unit cell has $N$ honeycomb lattice sites, which we here refer to as an $N$-ZMDSN. (b) The band structure of a 48-ZMDSN. The inset specifies the lowest-energy subbands in terms of different edge and spin states. The mirror image of each subband with respect to the vertical dashed line at $k_x = \pi/a$ is associated with a spin inversion. Therefore, the edge states possess a right-handed helicity [25].

### B. Dissipationless quantum transport

For quantum transport simulations we focus only on a nondissipative regime in which no inelastic scattering occurs

TABLE I. Matrix elements of the hopping parameters between nearest Mo-Mo, Mo-S, and S-S atoms. All the matrices are obtained in the spirit of the Slater-Koster tight-binding model [23,24]. Each element is then a linear function of hopping integrals and overlap parameters, e.g., $[t_1^{MM}(V_{dd\delta}, V_{dd\pi}, V_{dd\sigma})]_{11} = v_1 V_{dd\delta} + v_2 V_{dd\pi} + v_3 V_{dd\sigma}$, where the subscript in $t_1^{MM}$ corresponds to the hopping direction $a_1$ in Fig. 1(a) and $v_1$, $v_2$, $v_3$ are coefficients. These coefficients are separately specified for each element using the same notation. The hopping integrals (in eV) are as follows [23]: $V_{pd\pi} = -1.241$, $V_{pd\sigma} = 3.689$, $V_{dd\delta} = 0.228$, $V_{dd\pi} = 0.252$, $V_{dd\sigma} = -0.895$, $V_{pp\pi} = -0.467$, and $V_{pp\sigma} = 1.225$.

| | Elements | | | | | | | | |
|---|---|---|---|---|---|---|---|---|---|
| Hopping matrix (arguments) | $[...]_{11}$ | $[...]_{12}$ | $[...]_{13}$ | $[...]_{21}$ | $[...]_{22}$ | $[...]_{23}$ | $[...]_{31}$ | $[...]_{32}$ | $[...]_{33}$ |
| $t_1^{MM}(V_{dd\delta}, V_{dd\pi}, V_{dd\sigma})$ | $\frac{3}{4},0,\frac{1}{4}$ | $-\frac{\sqrt{3}}{8},0,\frac{\sqrt{3}}{8}$ | $-\frac{3}{8},0,\frac{3}{8}$ | $-\frac{\sqrt{3}}{8},0,\frac{\sqrt{3}}{8}$ | $\frac{1}{16},\frac{3}{4},\frac{3}{16}$ | $\frac{\sqrt{3}}{16},-\frac{\sqrt{3}}{4},\frac{3\sqrt{3}}{16}$ | $-\frac{3}{8},0,\frac{3}{8}$ | $\frac{\sqrt{3}}{16},-\frac{\sqrt{3}}{4},\frac{3\sqrt{3}}{16}$ | $\frac{3}{16},\frac{1}{4},\frac{9}{16}$ |
| $t_2^{MM}(V_{dd\delta}, V_{dd\pi}, V_{dd\sigma})$ | $\frac{3}{4},0,\frac{1}{4}$ | $\frac{\sqrt{3}}{4},0,-\frac{\sqrt{3}}{4}$ | 0,0,0 | $\frac{\sqrt{3}}{4},0,-\frac{\sqrt{3}}{4}$ | $\frac{1}{4},0,\frac{3}{4}$ | 0,0,0 | 0,0,0 | 0,0,0 | 0,1,0 |
| $t_3^{MM}(V_{dd\delta}, V_{dd\pi}, V_{dd\sigma})$ | $\frac{3}{4},0,\frac{1}{4}$ | $-\frac{\sqrt{3}}{8},0,\frac{\sqrt{3}}{8}$ | $\frac{3}{8},0,-\frac{3}{8}$ | $-\frac{\sqrt{3}}{8},0,\frac{\sqrt{3}}{8}$ | $\frac{1}{16},\frac{3}{4},\frac{3}{16}$ | $-\frac{\sqrt{3}}{16},\frac{\sqrt{3}}{4},-\frac{3\sqrt{3}}{16}$ | $\frac{3}{8},0,-\frac{3}{8}$ | $-\frac{\sqrt{3}}{16},\frac{\sqrt{3}}{4},-\frac{3\sqrt{3}}{16}$ | $\frac{3}{16},\frac{1}{4},\frac{9}{16}$ |
| $t_1^{MS}(V_{pd\pi}, V_{pd\sigma})$ | $-\frac{9\sqrt{2}}{7\sqrt{7}},\frac{\sqrt{6}}{7\sqrt{7}}$ | $\frac{3\sqrt{6}}{7\sqrt{7}},-\frac{\sqrt{2}}{7\sqrt{7}}$ | $\frac{12\sqrt{2}}{7\sqrt{7}},\frac{\sqrt{6}}{7\sqrt{7}}$ | $\frac{5\sqrt{6}}{7\sqrt{7}},\frac{3\sqrt{2}}{7\sqrt{7}}$ | $\frac{9\sqrt{2}}{7\sqrt{7}},-\frac{\sqrt{6}}{7\sqrt{7}}$ | $-\frac{2\sqrt{6}}{7\sqrt{7}},\frac{3\sqrt{2}}{7\sqrt{7}}$ | $-\frac{\sqrt{2}}{7\sqrt{7}},-\frac{3\sqrt{6}}{7\sqrt{7}}$ | $\frac{5\sqrt{6}}{7\sqrt{7}},\frac{3\sqrt{2}}{7\sqrt{7}}$ | $\frac{6\sqrt{2}}{7\sqrt{7}},-\frac{3\sqrt{6}}{7\sqrt{7}}$ |
| $t_2^{MS}(V_{pd\pi}, V_{pd\sigma})$ | 0,0 | $-\frac{6\sqrt{6}}{7\sqrt{7}},\frac{2\sqrt{2}}{7\sqrt{7}}$ | $\frac{12\sqrt{2}}{7\sqrt{7}},\frac{\sqrt{6}}{7\sqrt{7}}$ | 0,0 | $-\frac{6\sqrt{2}}{7\sqrt{7}},-\frac{4\sqrt{6}}{7\sqrt{7}}$ | $\frac{4\sqrt{6}}{7\sqrt{7}},-\frac{6\sqrt{2}}{7\sqrt{7}}$ | $\frac{14\sqrt{2}}{7\sqrt{7}},0$ | 0,0 | 0,0 |
| $t_3^{MS}(V_{pd\pi}, V_{pd\sigma})$ | $\frac{9\sqrt{2}}{7\sqrt{7}},-\frac{\sqrt{6}}{7\sqrt{7}}$ | $\frac{3\sqrt{6}}{7\sqrt{7}},-\frac{\sqrt{2}}{7\sqrt{7}}$ | $\frac{12\sqrt{2}}{7\sqrt{7}},\frac{\sqrt{6}}{7\sqrt{7}}$ | $-\frac{5\sqrt{6}}{7\sqrt{7}},-\frac{3\sqrt{2}}{7\sqrt{7}}$ | $\frac{9\sqrt{2}}{7\sqrt{7}},-\frac{\sqrt{6}}{7\sqrt{7}}$ | $-\frac{2\sqrt{6}}{7\sqrt{7}},\frac{3\sqrt{2}}{7\sqrt{7}}$ | $-\frac{\sqrt{2}}{7\sqrt{7}},-\frac{3\sqrt{6}}{7\sqrt{7}}$ | $-\frac{5\sqrt{6}}{7\sqrt{7}},-\frac{3\sqrt{2}}{7\sqrt{7}}$ | $-\frac{6\sqrt{2}}{7\sqrt{7}},\frac{3\sqrt{6}}{7\sqrt{7}}$ |
| $t_1^{SS}(V_{pp\pi}, V_{pp\sigma})$ | $\frac{3}{4},\frac{1}{4}$ | $\frac{\sqrt{3}}{4},-\frac{\sqrt{3}}{4}$ | 0,0 | $\frac{\sqrt{3}}{4},-\frac{\sqrt{3}}{4}$ | $\frac{1}{4},\frac{3}{4}$ | 0,0 | 0,0 | 0,0 | 1,0 |
| $t_2^{SS}(V_{pp\pi}, V_{pp\sigma})$ | 0,1 | 0,0 | 0,0 | 0,0 | 1,0 | 0,0 | 0,0 | 0,0 | 1,0 |
| $t_3^{SS}(V_{pp\pi}, V_{pp\sigma})$ | $\frac{3}{4},\frac{1}{4}$ | $-\frac{\sqrt{3}}{4},\frac{\sqrt{3}}{4}$ | 0,0 | $-\frac{\sqrt{3}}{4},\frac{\sqrt{3}}{4}$ | $\frac{1}{4},\frac{3}{4}$ | 0,0 | 0,0 | 0,0 | 1,0 |

inside the transport channel shown in Fig. 1(a). A typical mechanism that can largely push the system out of this regime is phonon interactions, which are avoided here with the assumption that temperature is very low. It is also worth mentioning that the calculated mean free path for $MoS_2$ monolayers is about 14–18 nm at room temperature [32,33]. Therefore, the length of the channel region will be much smaller than the mean free path, provided that it consists of only a few unit cells, which is the required condition for ballistic transport. This allows us to use the Landauer formula in order to evaluate the spin-resolved conductance, that is,

$$G^s(E) = \frac{e^2}{h} T^s(E). \tag{5}$$

Here, $T^s$ denotes the probability that an electron injected from the left terminal will transmit with spin $s$ to the right terminal. The transmission function can then be calculated in terms of the Green's function of the transport channel

$$T^s(E) = \mathrm{Tr}\left(\Gamma_L^s \mathcal{G}^s \Gamma_R^s \mathcal{G}^{s\dagger}\right), \tag{6}$$

with $\mathcal{G}^s$ representing the retarded Green's function for spin $s$ and

$$\Gamma_{L(R)}^s = i\left(\Sigma_{L(R)}^s - \Sigma_{L(R)}^{s\dagger}\right), \tag{7}$$

the broadening matrix due to strong couplings with the left- (right-) handed terminal. To calculate the self-energy, the Green's function at lead-channel contact regions is required. For the contact point at $l = 0$ we find

$$\Sigma_L^s = H_{01}^\dagger \mathcal{G}_{00}^s H_{01}. \tag{8}$$

TABLE II. On-site tight-binding parameters (in eV) [23].

| $\Delta_0$ | $\Delta_2$ | $\Delta_p$ | $\Delta_z$ | $t_{zz}^\perp$ | $t_{vv}^\perp$ $(v = x, y)$ |
|---|---|---|---|---|---|
| −1.094 | −1.512 | −3.560 | −6.886 | 1.225 | −0.467 |

Assuming that the left lead is homogeneous, i.e., $H_{00} = H_{\text{-}1\text{-}1}, \ldots$ and $H_{\text{-}10} = H_{\text{-}2\text{-}1}, \ldots$, the Green's function due to an excitation at $l = 0$, $\mathcal{G}_{00}^s(E)$, can be obtained via a set of coupled equations as detailed below:

$$\begin{aligned}
(E + i\eta - H_{00})\mathcal{G}_{00}^s &= \mathbf{I} + H_{\text{-}10}^\dagger \mathcal{G}_{\text{-}10}^s, \\
(E + i\eta - H_{00})\mathcal{G}_{\text{-}10}^s &= H_{\text{-}10}^\dagger \mathcal{G}_{\text{-}20}^s + H_{\text{-}10}\mathcal{G}_{00}^s, \\
&\cdots, \\
(E + i\eta - H_{00})\mathcal{G}_{\text{-}n0}^s &= H_{\text{-}10}^\dagger \mathcal{G}_{\text{-}n\text{-}1,0}^s + H_{\text{-}10}\mathcal{G}_{\text{-}n+1,0}^s,
\end{aligned} \tag{9}$$

where $\eta$ is an infinitesimal real constant. Owing to the countless number of iterative cells in semi-infinite leads, finding a solution to the set of equations (9) would be very cumbersome without the implementation of a proper algorithm [34–36]. To tackle this problem we employ an elegant approach that was first introduced for the calculation of the surface Green's function in a crystal of stacked layers [34]. The fundamental hypothesis of this method is that the Green's function of each unit cell (layer) can be expressed in terms of the preceding or next one, i.e., $\mathcal{G}_{\text{-}10}^s = \bar{\mathcal{T}}\mathcal{G}_{00}^s$, or, equivalently, $\mathcal{G}_{00}^s = \mathcal{T}\mathcal{G}_{\text{-}10}^s$. Here, $\mathcal{T}$ and $\bar{\mathcal{T}}$ are transfer matrices that can be computed from the coupling between two adjacent unit cells $H_{l,l+1}$ via the following iterative scheme:

$$\mathcal{T} = t_0 + t_0\widetilde{t}_1 + t_0 t_1 \widetilde{t}_2 + \cdots + t_0 t_1 t_2 \cdots \widetilde{t}_n, \tag{10}$$

$$\bar{\mathcal{T}} = \widetilde{t}_0 + \widetilde{t}_0 t_1 + \widetilde{t}_0\widetilde{t}_1 t_2 + \cdots + \widetilde{t}_0\widetilde{t}_1\widetilde{t}_2 \cdots t_n, \tag{11}$$

where $t_i$ and $\widetilde{t}_i$ are defined through the recursion equations

$$t_i = (\mathbf{I} - \widetilde{t}_{i-1}t_{i-1} - t_{i-1}\widetilde{t}_{i-1})^{-1} t_{i-1}^2, \tag{12}$$

$$\widetilde{t}_i = (\mathbf{I} - \widetilde{t}_{i-1}t_{i-1} - t_{i-1}\widetilde{t}_{i-1})^{-1} \widetilde{t}_{i-1}^2, \tag{13}$$

and

$$t_0 = (E + i\eta - H_{00})^{-1} H_{\text{-}10}^\dagger, \tag{14}$$

$$\widetilde{t}_0 = (E + i\eta - H_{00})^{-1} H_{-10}. \quad (15)$$

The infinite sum in Eqs. (10) and (11) can be truncated as soon as the transmission functions are converged. On this basis, the Green's function at site $l = 0$ of the left lead takes the form

$$\mathcal{G}^s_{00}(E) = [(E + i\eta)\mathbf{I} - H_{00} - H^{\dagger}_{-10}\bar{\mathcal{T}}]^{-1}. \quad (16)$$

Along the same lines as in Eqs. (8)–(16) one can calculate the self-energy due to scatterings into the right lead. For any arbitrary unit cell inside the transport channel, the Green's function can be computed by translating $\mathcal{G}^s_{00}(E)$ step by step forward as follows:

$$\mathcal{G}^s_{l+1,0} = [(E + i\eta)\mathbf{I} - H_{l,l} - H^{\dagger}_{l,l+1}\mathcal{G}^s_{l,0}H_{l,l+1}]^{-1}. \quad (17)$$

Note that this approach has been employed before in order to investigate low-temperature transport in carbon nanotubes [35] as well as in silicene nanoribbons [36].

## III. RESULTS

Many electronic properties of 2D hexagonal crystals are shown to depend on their edge structure. This dependency can be more pronounced for $MoS_2$ nanoribbons, especially if they are terminated by zigzag edges, because the constituent atoms of the opposite edges would not be chemically equivalent [see Fig. 1(a)]. We further show that the imbalance of the opposite edges is a key element for the determination of the electronic properties of ZMDSNs.

The electronic structure of a 48-ZMDSN is depicted in Fig. 1(b). The lowest-energy subbands indicate four metallic states residing on the zigzag edges and hence are labeled by both the edge and spin quantum numbers. For brevity, we hereafter specify the two edges by their atom type as "$X$ edge", where $X =$ Mo or S. As seen from Fig. 1(b), depending on the nature of edge atoms, the metallic modes exhibit electron- and holelike band dispersions for the S edge and Mo edge, respectively [21]. Similar to graphene-based zigzag nanoribbons, the edges of ZMDSNs are indeed the only conductive channels hosting the metallic states. However, contrary to the electronic structure of zigzag graphene nanoribbons, we find that the band dispersion of these states is no longer flat in ZMDSNs. Near the crossing points seen in Fig. 1(b) the band dispersion resembles very closely that of massless Dirac fermions. Neglecting the duality of these crossings on both sides of $k_x = \pi/a$, a similar linear dispersion has previously been perceived for topological modes of Hg(Cd)Te heterostructures [37] (these materials provide a convenient platform for the observation of the quantum spin Hall effect [38] and spin-polarized quantum Hall liquids [39]). This similarity can be traced back to the fact that either the effective Hamiltonian of $MoS_2$ monolayers or that of Hg(Cd)Te quantum wells, which is known as the Bernevig-Hughes-Zhang (BHZ) model [40], includes $k^2$- and $k$-dependent terms [18,19] and that the sizable band gap of their bulk structure is due to a mass parameter. Because Hg(Cd)Te heterostructures lack the valley degree of freedom, time-reversal symmetry results in two degenerate states (Kramers doublets) that are only tagged by their spin orientation. Such spin-polarized metallic modes propagate in opposite directions, giving rise to a quantum spin Hall effect. Conversely, Fig. 1(b) shows that both opposite spins move

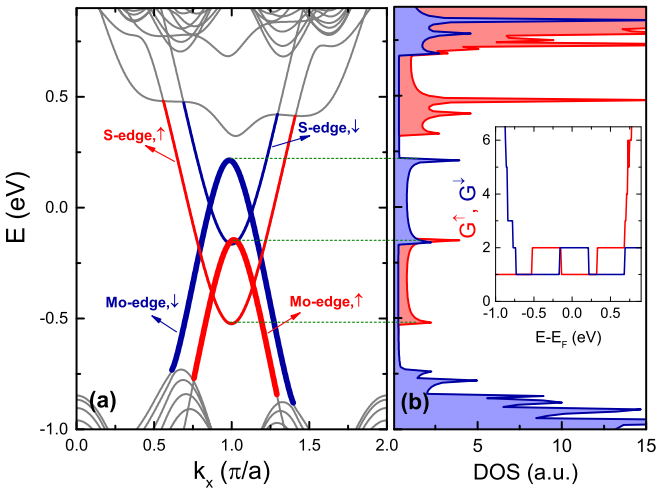


FIG. 2. (a) The energy band dispersion of a 48-ZMDSN for an exchange interaction of strength $h = 2.4\lambda_M$. The thick (thin) colored curves indicate two in-gap states localized on the Mo edge (S edge). For clarity, the spin-up and spin-down states are shown in red and blue, respectively. (b) Corresponding spin-polarized density of states. The van Hove singularities are seen as sharp peaks coinciding with the onset of energy subbands. The inset shows the spin-resolved conductance as a function of the energy of the incoming electrons.

in the same direction near the crossings. As a result, the separation of charge carriers in terms of the spin degree of freedom with the help of the quantum Hall effect seems to be not feasible.

One of the conventional techniques often used to unbalance the reverse spins is to induce an exchange field that can emerge due to the proximity effect by ferromagnetic insulators. Consequently, the spin characteristics of the 2D system are mostly determined by the majority spin near the Fermi energy level. The band dispersion of a 48-ZMDSN for an exchange field of $h = 2.4\lambda_M$ [31] is shown in Fig. 2. Contrary to the intrinsic spin-orbit coupling of $MoS_2$ monolayers which splits the band structure parallel to the $k_x$ direction [see Fig. 1(b)], the nonparallel spins are now shifted inversely on the $E$ axis. Given the fact that the band structure repeats itself under translations $k_x \to k_x + 2n\pi/a$ ($n = \pm 1, \pm 2, \ldots$), which is further supported by the Bloch periodic boundary condition in Eq. (4), one can easily prove that $E_{s,k_x} = E_{-s,-k_x} - 2sh$; for more details we refer to Ref. [25]. This means that the presence of an exchange field breaks spin inversion symmetry with respect to the $k_x = 0$ axis [according to the argument made in Ref. [25], the equality $E_{s,k_x} = E_{-s,-k_x}$ is tantamount to the right-handed helicity as depicted in Fig. 1(b)]. The direct consequence of this asymmetry for the density of states, $\mathrm{DOS}(s,E) = -\frac{1}{\pi}\mathrm{Im\,Tr}[\mathcal{G}^s(E)]$, is the emergence of spin-polarized van Hove peaks, which are clearly seen in Fig. 2(b). Note that although the field $h$ shifts nonparallel spins in opposite directions, the Mo- and S-edge modes are still equivalent in terms of the overall energy change. In spite of the giant spin splitting induced by $h$, no energy gap is induced between any two successive subbands with the same spin. As a result, neither the spin-up contribution nor the spin-down contribution vanishes in the conductance, as shown in the

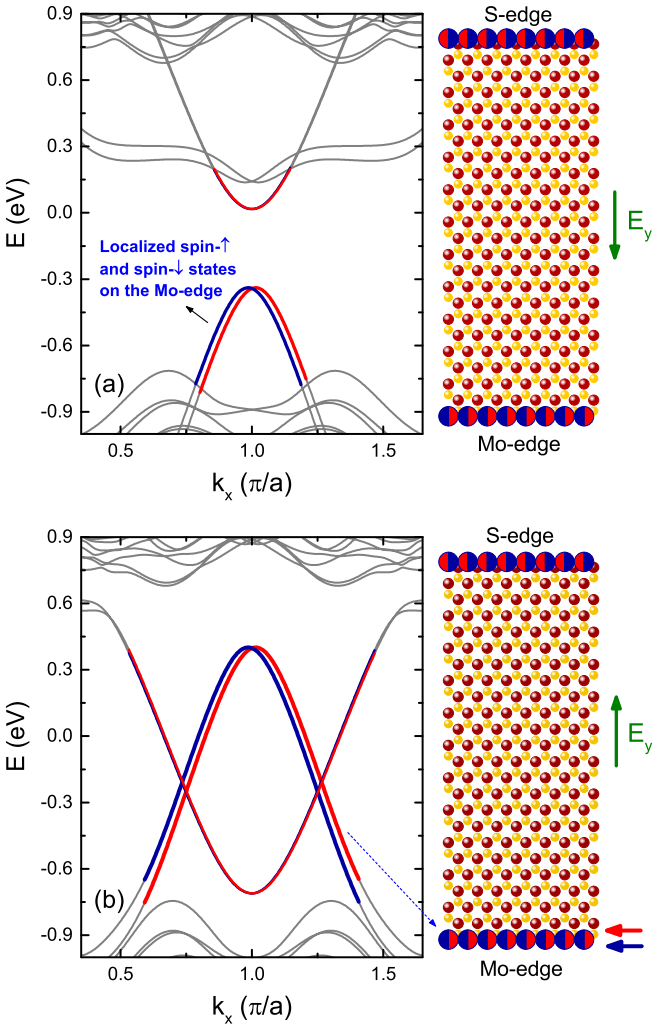


FIG. 3. The band structure of a 48-ZMDSN subject to a transverse electric field. (a) and (b) show the energy dispersion of low-energy subbands for two inverse fields, $E_y = -0.75$ V$/w$ and $E_y = 0.75$ V$/w$, respectively, where $w$ is the ribbon width. The electrical function of the ZMDSN is strongly field dependent and can range from (a) semiconducting to (b) metallic phase. The directions of motion for spin-↑ and spin-↓ states on either Mo edge or S edge are identical.

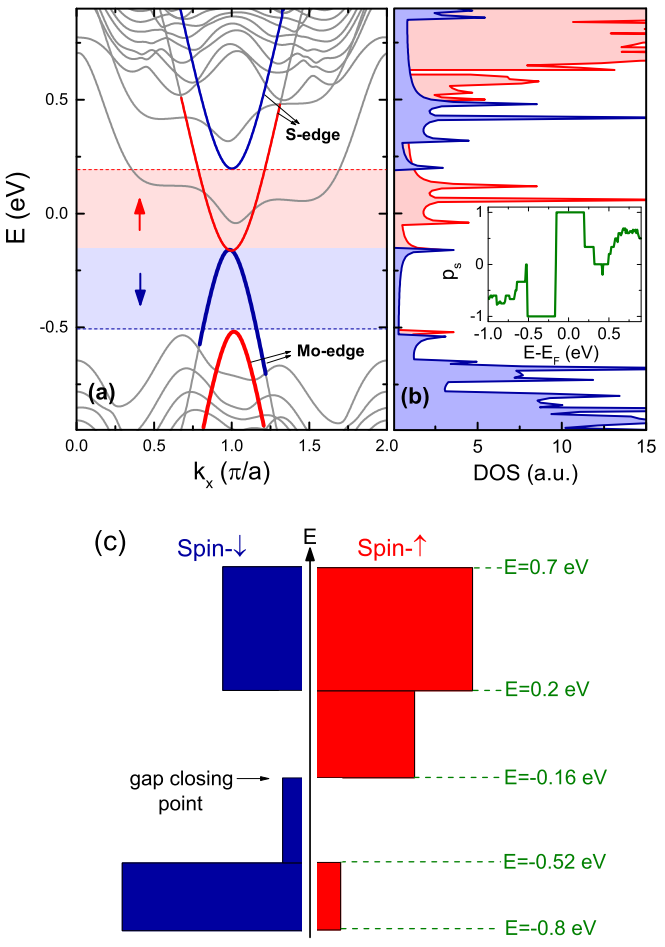


FIG. 4. (a) The electronic structure of a 48-ZMDSN when both transverse electric and exchange fields are applied simultaneously. The strength of the fields is set to $E_y = -0.75$ V$/w$ and $h = 2.4\lambda_M$. The colored domains between $E \approx -0.52$ and 0.2 eV show two exceptional regions in which the band structure is fully polarized in terms of the spin degree of freedom. At the gap-closing point the dominant spin orientation changes at once (↑⇌↓). (b) The density of energy states for different spin quantum numbers. The inset indicates the spin polarization $p_s$ as a function of the energy of incoming electrons. (c) The average $\overline{\text{DOS}}$ for opposite spins in different energy ranges. The ZMDSN acts like an insulator between $\approx -0.52$ and $-0.16$ eV for spin up and between $\approx -0.16$ and 0.2 eV for the spin-down state.

inset of Fig. 2(b), which prevents the realization of fully spin polarized transport.

The idea to achieve a 2D half-metal crystal, which allows for spin-selective transport, has been conceivable for zigzag graphene nanoribbons subject to a transverse electric field [41]. Here, with applied transverse electric field $\mathbf{E} = (0, E_y, 0)$, we observe an anomalous duality in the behavior of ZMDSNs. To be precise, depending on the sign of $E_y$, the band structure of a ZMDSN can offer either semiconducting or metallic properties. The results are shown in Fig. 3. This is indeed one of the significant consequences arising from the dissimilarity in the chemical natures of the opposite edges. Given the fact that sulfur atoms are electronegative, the application of a positive (negative) electrical gate on molybdenum atoms with respect to sulfur atoms can facilitate (suppress) the electron transferability between Mo-S bonds. Therefore, the electrical function of ZMDSNs would be unexpectedly incompatible for $E_y$ and $-E_y$ even though electrons are transmitted in the $x$ direction. Nevertheless, even with such contradictory behaviors in response to a transverse electric field, the edge modes are still degenerate in terms of the spin degree of freedom. From the subbands illustrated in Fig. 3, one can infer the same spin inversion as in Fig. 1(b), i.e., $E_{s,k_x} = E_{-s,-k_x}$, irrespective of which side the orientation of $E_y$ is. To better appreciate this similarity, it might be enough to recall that a transverse electric field keeps the periodicity of ZMDSNs unchanged along the repetition direction of the unit cells.

Figure 4 displays the electronic structure of a 48-ZMDSN when both the $\mathbf{E}$ and $h$ fields are applied simultaneously. The strength of the electric field is assumed to be $E_y = 0.75$ V$/w$

TABLE III. Required transverse electric field for a given $h$ field in order to induce the same half-metallic state as in Fig. 4. The results are given for a 48-ZMDSN with $w = 6.385$ nm. The size of the spin gap $\Delta s$ is almost identical for both spins.

| $h/\lambda_M$ | $\lvert\mathbf{E}\rvert$ (V/$w$) | $\Delta s$ (meV) |
|---|---|---|
| 0.1 | 0.4 | ∼15 |
| 0.5 | 0.46 | ∼75 |
| 1.0 | 0.54 | ∼150 |
| 2.0 | 0.69 | ∼300 |

($w$ is the ribbon width), so its tendency is towards the Mo edge. As seen, the wide band gap between the conduction and valence bulk states has been closed by two spin-polarized metallic states, each of which belongs to a disparate edge. The lower half of the band gap (the blue shaded region) is covered by a |Mo-edge, spin-↓⟩ state, but midway to the top both the edge and spin directions are suddenly inverted. By evaluating the spin-polarized conductance with the help of Eq. (5), the spin polarization of a current flowing through the $MoS_2$ channel can be calculated by $p_s(E) = (G^{\uparrow} - G^{\downarrow})/\sum_{s=\uparrow,\downarrow} G^s$. The obtained $p_s$, shown in the inset of Fig. 4(b), confirms that the conductance between $E \approx -0.52$ and 0.2 is completely spin polarized. In comparison to a perfect metallic system which allows electrons of all degrees of freedom to transmit, here the ZMDSN blocks electrons of one spin direction. The direction of the filtered spin critically depends on whether the energy of transmitted electrons is below or above the gap-closing point at $E \approx -0.16$ eV. Therefore, the ZMDSN acts as a metal for one spin direction but as an insulator for the opposite spin direction, which can be tuned by an external gate voltage. This can be interpreted as an indication of the fact that the ZMDSN has become a tunable half-metal structure. To establish the half-metallicity, we plot in Fig. 4(c) the average spin-polarized DOS, i.e., $\overline{\mathrm{DOS}}_{ab} = \int_{E_a}^{E_b} \mathrm{DOS}(E)\, dE/(E_b - E_a)$, for a few energy ranges corresponding to the band structure in Fig. 4(a). There are two nonparallel spin gaps which emerge above and below the gap-closing region. Such sizable spin gaps imply that, by applying an appropriate gate voltage to the ZMDSN, one can suppress the transmission of one spin direction in favor of its opposite counterpart. Note that the half-metal state of Fig. 4 can also be observed for lower $h$ fields (for an example, see Table III). According to Table III, one can infer that the size of the induced spin gap is approximately proportional to the strength of the exchange field, that is, $\Delta s \propto h$. Also, the data presented in Table IV indicate that the required electric field for inducing the same half-metallic state as in Fig. 4 decreases for wider ZMDSNs, whereas the size of the created spin gap remains unchanged.

TABLE IV. Required transverse electric field for inducing a half-metallic state in an $N$-ZMDSN for $h = 2.4\lambda_M$. $w$ is the corresponding ribbon width. The size of the induced spin gap for all ribbons is $\Delta s \sim 360$ meV.

| $N$ | 16 | 24 | 32 | 48 | 80 | 96 |
|---|---|---|---|---|---|---|
| $\lvert\mathbf{E}\rvert$ (V/$w$) | 0.792 | 0.772 | 0.765 | 0.754 | 0.748 | 0.746 |

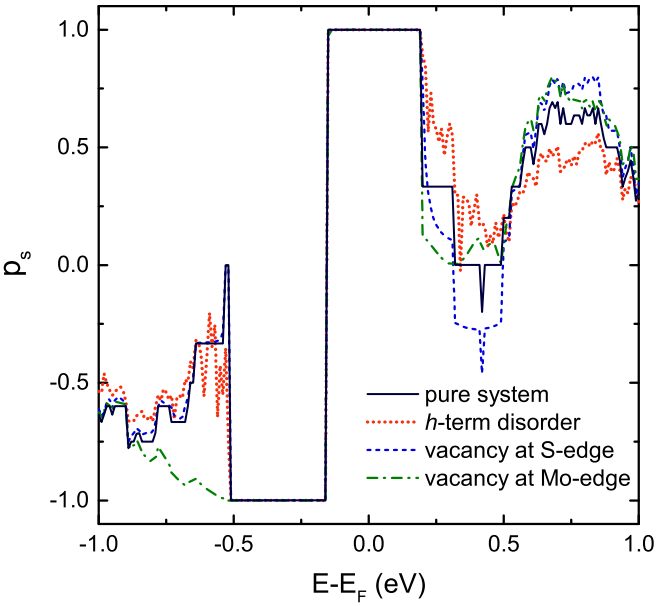


FIG. 5. The spin polarization $p_s$ as a function of the energy of incoming electrons in the presence of an edge defect or random $h$-field fluctuations.

The realization of an ideal uniform exchange field demands a defectless ferromagnetic insulator beneath the ZMDSN. In addition, the arrangement of all the Mo-S bonds has to be completely perfect, without any ripple or distortion. However, in practice, the fulfillment of both criteria seems to be technically very complicated and unlikely. The absence of such ideal conditions might disturb the strength of the exchange field spatially. Here, we model the exchange-field disturbance by random tiny fluctuations about its strength $h$. The maximum deviation from the average exchange field will be then a small fraction of it, i.e., $\delta h_{\max}/h \ll 1$. The spin polarization of the conductance spectrum $p_s$ in the presence of a randomly disordered $h$ field is shown in Fig. 5 by the red dotted line. To ensure that the results are valid and generalizable to any random sample of $h$, the shown $p_s$ has been averaged over the results of an ensemble of 100 independent samples. The average exchange field in all these samples is $h = 2.4\lambda_M$, and the maximum deviation $\delta h_{max}/h = 0.1$. The $p_s$ variations of a pure ZMDSN are also shown by the black solid line for reference. Despite the appearance of a superficial oscillatory structure, specifically near the steplike variations of $p_s$, the perfect spin polarization between $\approx -0.52$ and 0.2 eV, namely, the colored region in Fig. 4(a), is left unchanged. Therefore, one can reasonably conclude that the induced half-metallicity is robust against random deviations from the average exchange field. A similar conclusion can be drawn for edge defects, e.g., when a lattice site on the edge is vacant, which is one of the prevalent defects that usually affect the edges of 2D hexagonal structures. Physically, a vacancy can be modeled within the tight-binding method by tending the corresponding on-site energy to infinity. Comparing the $p_s$ curves of defected and pure ZMDSNs reveals that the fully polarized regions of the conductance spectrum cannot be influenced by an edge vacancy. It is also interesting to note that the presence of lattice vacancies in the ribbon's bulk region has no consequence

for the edge states, and hence, the induced half-metallicity is naturally immune to this kind of defect.

## IV. SUMMARY

We focused on the evolution of the edge states of ZMDSNs in response to a transverse electric field and/or an external exchange field. For a field-free ZMDSN it was shown that the band structure consists of four metallic edge modes with a right-handed helicity. Therefore, the spin of any particle belonging to these states is in the same direction as its momentum. The origin of this helicity is attributed to the lattice periodicity and the fact that the spin-orbit coupling Hamiltonian under a momentum reversal can be conserved via a spin inversion. With the presence of only an exchange or electric field, the electronic structure of the metallic edge modes does not yield any spin gap. We have shown that a ZMDSN in response to a transverse electric field can offer either metallic or insulating properties, but the helicity characteristics for either case remain unchanged. With the simultaneous application of both fields, we predict that a peculiar half-metallic state can be observed. The peculiarity of such spin-selective states is due to the fact that the allowed spin orientation can be easily controlled by an external gate voltage. We also showed that the induced half-metal phase is robust against the presence of edge vacancies or random deviations of the exchange field from its mean value.


[1] K. S. Novoselov, A. K. Geim, S. V. Morozov, D. Jiang, M. I. Katsnelson, I. V. Grigorieva, S. V. Dubonos, and A. A. Firsov, Nature (London) **438**, 197 (2005).

[2] Y. Zheng, Y. W. Tan, H. L. Stormer, and P. Kim, Nature (London) **438**, 201 (2005).

[3] A. Kuc, N. Zibouche, and T. Heine, Phys. Rev. B **83**, 245213 (2011).

[4] K.-K. Liu, W. Zhang, Y.-H. Lee, Y.-C. Lin, M.-T. Chang, C.-Y. Su, C.-S. Chang, H. Li, Y. Shi, H. Zhang, C.-S. Lai, and L.-J. Li, Nano Lett. **12**, 1538 (2012).

[5] Q. H. Wang, K. Kalantar-Zadeh, A. Kis, J. N. Coleman, and M. S. Strano, Nat. Nanotechnol. **7**, 699 (2012).

[6] Z. Y. Zhu, Y. C. Cheng, and U. Schwingenschlögl, Phys. Rev. B **84**, 153402 (2011).

[7] O. Lopez-Sanchez, D. Lembke, M. Kayci, A. Radenovic, and A. Kis, Nat. Nanotechnol. **8**, 497 (2013).

[8] B. Radisavljevic, A. Radenovic, J. Brivio, V. Giacometti, and A. Kis, Nat. Nanotechnol. **6**, 147 (2011).

[9] B. Radisavljevic and A. Kis, Nat. Mater. **12**, 815 (2013).

[10] S. Kim, A. Konar, W. S. Hwang, J. H. Lee, J. Lee, J. Yang, C. Jung, H. Kim, J. B. Yoo, J. Y. Choi, Y. W. Jin, S. Y. Lee, D. Jena, W. Choi, and K. Kim, Nat. Commun. **3**, 1011 (2012).

[11] H. Wang, L. Yu, Y.-H. Lee, Y. Shi, A. Hsu, M. L. Chin, L.-J. Li, M. Dubey, J. Kong, and T. Palacios, Nano Lett. **12**, 4674 (2012).

[12] G.-B. Liu, W. Y. Shan, Y. G. Yao, W. Yao, and D. Xiao, Phys. Rev. B **88**, 085433 (2013).

[13] D. Xiao, G.-B. Liu, W. Feng, X. Xu, and W. Yao, Phys. Rev. Lett. **108**, 196802 (2012).

[14] Y.-C. Lin, D. O. Dumcenco, Y.-S. Huang, and K. Suenaga, Nat. Nanotechnol. **9**, 391 (2014).

[15] C. Zhang, A. Johnson, C.-L. Hsu, L.-J. Li, and C.-K. Shih, Nano Lett. **14**, 2443 (2014).

[16] A. Vojvodic, B. Hinnemann, and J. K. Norskov, Phys. Rev. B **80**, 125416 (2009).

[17] W. Zhou, X. Zou, S. Najmaei, Z. Liu, Y. Shi, J. Kong, J. Lou, P. M. Ajayan, B. I. Yakobson, and J.-C. Idrobo, Nano Lett. **13**, 2615 (2013).

[18] C. G. Petérfalvi, A. Kormányos, and G. Burkard, Phys. Rev. B **92**, 245443 (2015).

[19] H. Rostami, R. Asgari, and F. Guinea, arXiv:1511.07003.

[20] N. F. Q. Yuan, K. F. Mak, and K. T. Law, Phys. Rev. Lett. **113**, 097001 (2014).

[21] R.-L. Chu, G.-B. Liu, W. Yao, X. Xu, D. Xiao, and C. Zhang, Phys. Rev. B **89**, 155317 (2014).

[22] E. Cappelluti, R. Roldán, J. A. Silva-Guillén, P. Ordejón, and F. Guinea, Phys. Rev. B **88**, 075409 (2013).

[23] H. Rostami, R. Roldán, E. Cappelluti, R. Asgari, and F. Guinea, Phys. Rev. B **92**, 195402 (2015).

[24] H. Rostami and R. Asgari, Phys. Rev. B **91**, 075433 (2015).

[25] In Fig. 1(b), from the symmetry of the band structure with respect to the $k_x = \pi/a$ axis we find that $E_{s,\pi/a-k'_x} = E_{-s,\pi/a+k'_x}$. Using the Bloch periodicity of Eq. (4), all the energy subbands for $\pi/a < k_x$ can be translated by one reciprocal lattice period, $K = -2\pi/a$, to the first Brillouin zone. This yields $E_{s,\pi/a-k'_x} = E_{-s,-\pi/a+k'_x}$, which, for $k_x = \pi/a - k'_x$, is equivalent to $E_{s,k_x} = E_{-s,-k_x}$, demonstrating that $s \parallel k_x$. Considering the reverse effect of $h$ for opposite spins, we finally obtain $E_{s,k_x} = E_{-s,-k_x} - 2sh$.

[26] R. Roldán, M. P. López-Sancho, E. Cappelluti, J. A. Silva-Guillén, P. Ordejón, and F. Guinea, 2D Mater. **1**, 034003 (2014).

[27] A. G. Swartz, P. M. Odenthal, Y. Hao, R. S. Ruoff, and R. K. Kawakami, ACS Nano **6**, 10063 (2012).

[28] H. Haugen, D. Huertas-Hernando, and A. Brataas, Phys. Rev. B **77**, 115406 (2008).

[29] Z. Wang, C. Tang, R. Sachs, Y. Barlas, and J. Shi, Phys. Rev. Lett. **114**, 016603 (2015).

[30] Z. Qiao, W. Ren, H. Chen, L. Bellaiche, Z. Zhang, A. H. MacDonald, and Q. Niu, Phys. Rev. Lett. **112**, 116404 (2014).

[31] H. Li, J. Shao, D. Yao, and G. Yang, ACS Appl. Mater. Interfaces **6**, 1759 (2014).

[32] Y. Cai, J. Lan, G. Zhang, and Y.-W. Zhang, Phys. Rev. B **89**, 035438 (2014).

[33] K. Kaasbjerg, K. S. Thygesen, and K. W. Jacobsen, Phys. Rev. B **85**, 115317 (2012).

[34] M. P. Lopez Scancho, J. M. Lopez Sancho, and J. Rubio, J. Phys. F **14**, 1205 (1984).

[35] M. Buongiorno Nardelli, Phys. Rev. B **60**, 7828 (1999).

[36] Kh. Shakouri, H. Simchi, M. Esmaeilzadeh, H. Mazidabadi, and F. M. Peeters, Phys. Rev. B **92**, 035413 (2015).

[37] B. Büttner, C. X. Liu, G. Tkachov, E. G. Novik, C. Brüne, H. Buhmann, E. M. Hankiewicz, P. Recher, B. Trauzettel, S. C. Zhang, and L. W. Molenkamp, Nat. Phys. **7**, 418 (2011).

[38] M. König, S. Wiedmann, C. Brüne, A. Roth, H. Buh-mann, L. Molenkamp, X.-L. Qi, and S.-C. Zhang, Science **318**, 766 (2007).
[39] Kh. Shakouri and F. M. Peeters, Phys. Rev. B **92**, 045416 (2015).
[40] B. A. Bernevig, T. L. Hughes, and S.-C. Zhang, Science **314**, 1757 (2006).
[41] Y.-W. Son, M. L. Cohen, and S. G. Louie, Nature (London) **444**, 347 (2006).